Open Access

CrossMark

A hydro-geophysical simulator for fluid and mechanical processes in volcanic areas

Armando Coco[1,2]*, Gilda Currenti[3], Joachim Gottsmann[2], Giovanni Russo[4] and Ciro Del Negro[3]

*Correspondence:
acoco@brookes.ac.uk
[1] Department of Mechanical
Engineering and Mathematical
Sciences, Oxford Brookes University,
Wheatley campus, Oxford,
OX331HX, United Kingdom
[2] Department of Earth Sciences,
University of Bristol, Wills Memorial
Building, Queen's Road, Clifton,
Bristol, BS81RJ, United Kingdom
Full list of author information is
available at the end of the article

Abstract

Efficient and accurate hydrothermal and mechanical mathematical models in porous media constitute a fundamental tool for improving the understanding of the subsurface dynamics in volcanic areas. We propose a finite-difference ghost-point method for the numerical solution of thermo-poroelastic and gravity change equations. The main aim of this work is to study how the thermo-poroelastic solutions vary in a realistic description of a specific volcanic region, focusing on the topography and the heterogeneous structure of Campi Flegrei (CF) caldera (Italy). Our numerical approach provides the opportunity to explore different model configurations that cannot be taken into account using standard analytical models. Since the physics of the investigated hydrothermal system is similar to any saturated reservoir, such as oil fields or CO_2 reservoirs produced by sequestration, the model is generally applicable to the monitoring and interpretation of both deformation and gravity changes induced by other geophysical hazards that pose a risk to human activity.

Keywords: poroelasticity; finite difference; fluid flow

1 Introduction

Volcano geophysics focuses on integrating data from different monitoring techniques and developing numerical and physical models to explain the observations. The geophysical observations collected in volcanic areas are the surface expressions of processes that occur deeply within the volcanic edifice. Integration of different geophysical observations and mathematical models enables to identify renewed volcanic activities, forecast eruptions, and assess related hazards [1]. Unrest periods are defined as variations in the geophysical and geochemical state of the volcanic system with respect to the background behaviour. Usually, geophysical changes observed during unrest periods are modelled in terms of volume and pressure changes in a magma chamber embedded within an elastic medium [2–4]. Indeed, this approach often appears at odds with the complex processes accompanying volcanic unrest. Particularly, the interplay between magma chambers and hydrothermal systems may result in the heating and pressurization of hydrothermal fluids, which in turn induce ground deformation and variations in the rock and fluid properties [5–14]. A quantitative evaluation of this interaction is fundamental for a correct hazard assessment in volcanic areas.

A thermo-poroelastic numerical model is here proposed to jointly evaluate ground deformation and gravity changes caused by hydrothermal fluid circulation in complex media

with surface topography and mechanical heterogeneities in a 2D axis symmetric formulation.

Although the model is applicable to a generic volcanic system, in this paper we set up the model parametrisation on the Campi Flegrei caldera (CFc), a volcanic area situated to the west of Naples. After a long period of quiescence, two main uplift episodes (1969-72 and 1982-84) highlighted a reawakening phase of the CFc without culminating in an eruption [15]. The total amount of uplift of 3.5 m induced the evacuation of about 40,000 people from the town of Pozzuoli and surrounding areas. A slow subsidence followed the second uplift episode, periodically interrupted by mini-uplifts. Since 2006 CFc started uplifting again, with a particularly increased rate from 2011 [16, 17].

To reduce the uncertainty related to hydrothermal activities, significant complexities must be accounted when a mathematical model is adopted, such as real topography and mechanical heterogeneities, which are indeed neglected by most of existing models [12, 14, 18, 19]. In addition, highly efficient and accurate numerical solvers are required when a large number of simulation runs must be executed for a single simulation scenario, such as for optimization purposes related to geophysical data inversion or when the thermo-poroelastic response must be calculated at each time step in a coupled hydrothermal/mechanical model [20].

The thermo-poroelastic numerical method proposed in this paper is second order accurate and based on a finite-difference ghost-point discretization for complex geometries successfully adopted in [21] to solve elliptic equations and in [22] for elasto-static 2D problems with plane-strain assumptions. Here, the methods proposed in [21, 22] are extended to account for thermal expansion and pore pressure effects (caused by the perturbation of the hydrothermal system) in a 2D axis symmetric framework. Although a 3D model would be suitable to represent a more accurate scenario, the axis symmetric assumption is a reasonable approximation for representing caldera systems and volcano edifices in general, which are usually characterized by radial structures.

In order to avoid artifacts introduced by finite truncation of the domain, a coordinate transformation method is adopted in order to prescribe vanishing solutions at infinite distances maintaining the second order accuracy [22]. An extension of the multigrid solver described in [21, 22] is adopted as well.

Hydrothermal activity is simulated by TOUGH2, a well known multi-phase multi-component software for fluid flow and heat transfer in porous media [23]. The hydrothermal system is perturbed by injecting fluids of magmatic origin at the base of a central conduit for a prolonged period (until steady-state conditions), simulating the fumarolic activity at La Solfatara [24]. Following unrest periods are modelled by an increased injection rate. Variations in relevant geophysical signals (pore pressure, temperature and density) between the initial condition (steady-state) and unrest period are computed at each time step and fed into the thermo-poroelastic model (one-way coupling) to compute associated ground deformations and gravity changes. A similar one-way approach has been implemented at CF in previous works (*e.g.*, [12, 14, 19]).

The model proposed in this paper is widely applicable to a large number of relevant scientific and engineering problems for addressing subsurface flow and transport problems, such as geological carbon sequestration, nuclear waste disposal, energy production from geothermal, oil and gas reservoirs as well as methane hydrate deposits, environmental remediation, vadose zone hydrology. The coupling with the suite of TOUGH simulators

makes the model suitable for simulating and interpreting geophysical changes induced by a wide range of alterations in the subsurface flows, such as CO_2 sequestration and geothermal exploitation. However, the main scope of this paper is related to the methodology rather than the application to case studies and comparison with real data, and then the focus is restricted to the simulation of ground deformation and gravity changes in a generic volcanic area whose model parametrisation is set up on the Campi Flegrei caldera.

2 Hydro-geophysical model

The mathematical model is based on the governing equations of the thermo-poroelasticity theory (Mechanical model, Section 2.1.1), which describes the elastic response of a porous medium to the propagation of hot fluid through pores (Hydrothermal model, Section 2.4) by the effects of variations in pore pressure and temperature. Alterations in the gravity field associated to fluid density variations are evaluated by the model described in Section 2.1.2.

2.1 Thermo-poroelasticity model
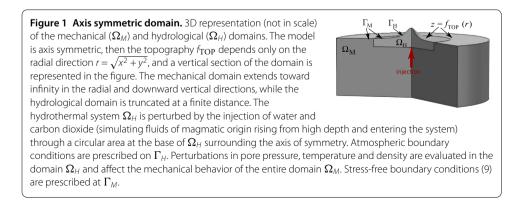
2.1.1 Mechanical model

Assuming that the deformation induced by pore pressure and temperature changes occurs slowly compared to the time scales of elastic waves, and that the system behaves as elastic (neglecting then the elasto-plastic and viscoelastic effects, which, to a first approximation, is a reasonable assumption for shallow crusts), the rock can be considered in static equilibrium and the displacement is found by solving the equations of equilibrium coupled with thermo-poroelastic extension of Hooke's law [25], giving the following set of equations [26]:

$$\nabla \cdot \boldsymbol{\sigma} = 0 \quad \text{in } \Omega_M,$$
$$\boldsymbol{\sigma} = \lambda \operatorname{tr}(\boldsymbol{\varepsilon})\boldsymbol{I} + 2\mu\boldsymbol{\varepsilon} + \alpha_{\mathrm{BW}}\Delta P\boldsymbol{I} + (3\lambda + 2\mu)\alpha\Delta T\boldsymbol{I}, \qquad (1)$$
$$\boldsymbol{\varepsilon} = \frac{1}{2}\big(\nabla\boldsymbol{u} + (\nabla\boldsymbol{u})^T\big),$$

where $\boldsymbol{\sigma}$ and $\boldsymbol{\varepsilon}$ are the stress and strain tensors, respectively, $\boldsymbol{u}$ is the deformation vector, λ and μ are the Lame's elastic medium parameters and $\boldsymbol{I}$ is the identity tensor. Eqs. (1) are solved in the domain Ω_M (the mechanical domain) for the unknown $\boldsymbol{u}$. In our simulations Ω_M is an infinite domain in the radial and downward vertical directions, *i.e.* $\Omega_M = \{(x, y, z) \in \mathbb{R}^3 : z < f_{\mathrm{TOP}}(x, y)\}$ (see Figure 1).

Figure 1 Axis symmetric domain. 3D representation (not in scale) of the mechanical (Ω_M) and hydrological (Ω_H) domains. The model is axis symmetric, then the topography f_{TOP} depends only on the radial direction $r = \sqrt{x^2 + y^2}$, and a vertical section of the domain is represented in the figure. The mechanical domain extends toward infinity in the radial and downward vertical directions, while the hydrological domain is truncated at a finite distance. The hydrothermal system Ω_H is perturbed by the injection of water and carbon dioxide (simulating fluids of magmatic origin rising from high depth and entering the system) through a circular area at the base of Ω_H surrounding the axis of symmetry. Atmospheric boundary conditions are prescribed on Γ_H. Perturbations in pore pressure, temperature and density are evaluated in the domain Ω_H and affect the mechanical behavior of the entire domain Ω_M. Stress-free boundary conditions (9) are prescribed at Γ_M.

A suitable set of boundary conditions is posed to close the mathematical problem, namely zero displacements at infinity and stress-free boundary conditions $\boldsymbol{\sigma} \cdot \boldsymbol{n}_s = 0$ on the ground surface $\Gamma_M = \{z = f_{\text{TOP}}(x, y)\}$.

Analyzing the stress tensor (second equation of (1)), we observe that two terms are added to the elastic stress tensor of the general Hooke's law: the ΔP pore-pressure contribution from poroelasticity theory through the α_{BW} Biot-Willis coefficient and the ΔT temperature contribution from thermo-elasticity theory through the linear thermal expansion coefficient α. Both ΔP and ΔT refer to perturbations with respect to a previous equilibrium state.

2.1.2 Gravity model

Fluid circulation, temperature and pore-pressure changes necessarily alter the fluid density distribution, which, in turn, affects the gravity field. Gravity variations in active volcanic areas range in amplitude between a few μGal (1 μGal = 10^{-8} m/s^2) and several hundred μGal with a spectrum varying from seconds to years depending on the involved subsurface mass-redistribution processes. The gravity change Δg, arising from fluid density redistribution, can be calculated by solving the following boundary value problem (Poisson equation) for the gravitational potential ϕ_g [27]:

$$\nabla^2 \phi_g = -4\pi G \Delta \rho \quad \text{in } \mathbb{R}^3,$$
$$\Delta g = -\frac{\partial \phi_g}{\partial z}, \tag{2}$$

where G is the gravitational constant and $\Delta \rho$ is the density distribution change. The problem is closed imposing the condition of vanishing gravitational potential at infinity. Density changes in the medium are computed with respect to an initial density distribution $\Delta \rho = \rho(\vec{x}, t) - \rho_0(\vec{x})$, where $\rho(\vec{x}, t) = \phi(\vec{x}, t) \sum_\beta \rho_\beta S_\beta$, with ϕ being the porosity, S_β and ρ_β the saturation and density of the phase β, respectively.

2.2 Axis symmetric formulation

In order to reduce the computational burden associated with 3D models we reformulate problems (1) and (2) in cylindrical coordinates and assume that they are axis symmetric, reducing then to a 2D formulation (Figure 1). We recall the coordinate transformation expressing the cylindrical coordinates (r, θ, z) in terms of Cartesian coordinates (x, y, z):

$$\begin{cases} x = r\cos(\theta), \\ y = r\sin(\theta), \quad r \geq 0, \theta \in [0, 2\pi], z \in \,]-\infty, +\infty[, \\ z = z, \end{cases}$$

where r, θ and z are the radial, angular and vertical coordinates, respectively. For simplicity, we maintain the same nomenclature for all quantities, even if they are expressed in cylindrical coordinates, $\{\boldsymbol{\sigma}, \boldsymbol{\varepsilon}, \boldsymbol{u}, \lambda, \mu, \Delta P, \Delta T, \Delta \rho\}(r, \theta, z), f_{\text{TOP}}(r, \theta)$.

The components of tensors $\boldsymbol{\sigma}$, $\boldsymbol{\varepsilon}$, $\boldsymbol{u}$ are named in such a way the cylindrical coordinate formulation is highlighted by a proper subscript, as follows.

$$\boldsymbol{\sigma} = (\sigma_{ij})_{i,j=r,\theta,z}, \qquad \boldsymbol{\varepsilon} = (\varepsilon_{ij})_{i,j=r,\theta,z}, \qquad \boldsymbol{u} = (u_i)_{i=r,\theta,z}.$$

Strain tensor ε components expressed in terms of $\boldsymbol{u}$ components read [25, 26]:

$$\varepsilon_{rr} = \frac{\partial u_r}{\partial r}, \qquad \varepsilon_{r\theta} = \frac{1}{2}\left(\frac{\partial u_\theta}{\partial r} + \frac{1}{r}\frac{\partial u_r}{\partial \theta} - \frac{u_\theta}{r}\right),$$

$$\varepsilon_{\theta\theta} = \frac{u_r}{r} + \frac{1}{r}\frac{\partial u_\theta}{\partial \theta}, \qquad \varepsilon_{\theta z} = \frac{1}{2}\left(\frac{1}{r}\frac{\partial u_z}{\partial \theta} + \frac{\partial u_\theta}{\partial z}\right), \tag{3}$$

$$\varepsilon_{zz} = \frac{\partial u_z}{\partial z}, \qquad \varepsilon_{rz} = \frac{1}{2}\left(\frac{\partial u_r}{\partial z} + \frac{\partial u_z}{\partial r}\right).$$

Stress-strain relationship presents the same functional formulation as in Cartesian coordinates, namely the second Eq. of (1):

$$\boldsymbol{\sigma} = \lambda\,\mathrm{tr}(\boldsymbol{\varepsilon})\boldsymbol{I} + 2\mu\boldsymbol{\varepsilon} + \alpha_{\mathrm{BW}}\Delta P\boldsymbol{I} + (3\lambda + 2\mu)\alpha\,\Delta T\boldsymbol{I}. \tag{4}$$

Using the cylindrical coordinates formulation of the divergence operator acting on a second order tensor field, Eq. (1) ($\nabla \cdot \boldsymbol{\sigma} = 0$) becomes [25, 26]:

$$\frac{1}{r}\frac{\partial \sigma_{\theta\theta}}{\partial \theta} + \frac{\partial \sigma_{r\theta}}{\partial r} + \frac{2\sigma_{r\theta}}{r} + \frac{\partial \sigma_{\theta z}}{\partial z} = 0,$$

$$\frac{\partial \sigma_{rr}}{\partial r} + \frac{1}{r}\frac{\partial \sigma_{r\theta}}{\partial \theta} + \frac{\sigma_{rr} - \sigma_{\theta\theta}}{r} + \frac{\partial \sigma_{rz}}{\partial z} = 0, \tag{5}$$

$$\frac{\partial \sigma_{zz}}{\partial z} + \frac{1}{r}\frac{\partial \sigma_{\theta z}}{\partial \theta} + \frac{\partial \sigma_{rz}}{\partial r} + \frac{\sigma_{rz}}{r} = 0.$$

The axis symmetric formulation corresponds to assuming that: (i) all quantities are independent of the angular coordinate θ, namely $\partial q/\partial \theta = 0$ for $q \in \{\sigma_{ij}, \varepsilon_{ij}, u_i, \lambda, \mu, \Delta P, \Delta T, f_{\mathrm{TOP}}\}$, (then they can be expressed only in terms of the radial and vertical coordinates by $q(r, z)$); and (ii) the displacement along the angular coordinates is zero (*i.e.* $u_\theta = 0$). By these assumptions, Eqs. (3) simplify to:

$$\varepsilon_{rr} = \frac{\partial u_r}{\partial r}, \qquad \varepsilon_{\theta\theta} = \frac{u_r}{r}, \qquad \varepsilon_{zz} = \frac{\partial u_z}{\partial z},$$

$$\varepsilon_{r\theta} = \varepsilon_{\theta z} = 0, \qquad \varepsilon_{rz} = \frac{1}{2}\left(\frac{\partial u_r}{\partial z} + \frac{\partial u_z}{\partial r}\right). \tag{6}$$

Using (4) and (6), the stress components become (observe that $\sigma_{\theta\theta}$ is not necessarily zero):

$$\sigma_{rr} = \frac{2\mu}{1 - 2\nu}\left[(1 - \nu)\frac{\partial u_r}{\partial r} + \nu\left(\frac{u_r}{r} + \frac{\partial u_z}{\partial z}\right)\right] + \alpha_{\mathrm{BW}}\Delta P + (3\lambda + 2\mu)\alpha\,\Delta T,$$

$$\sigma_{\theta\theta} = \frac{2\mu}{1 - 2\nu}\left[(1 - \nu)\frac{u_r}{r} + \nu\left(\frac{\partial u_r}{\partial r} + \frac{\partial u_z}{\partial z}\right)\right] + \alpha_{\mathrm{BW}}\Delta P + (3\lambda + 2\mu)\alpha\,\Delta T,$$

$$\sigma_{zz} = \frac{2\mu}{1 - 2\nu}\left[(1 - \nu)\frac{\partial u_z}{\partial z} + \nu\left(\frac{\partial u_r}{\partial r} + \frac{u_r}{r}\right)\right] + \alpha_{\mathrm{BW}}\Delta P + (3\lambda + 2\mu)\alpha\,\Delta T, \tag{7}$$

$$\sigma_{r\theta} = \sigma_{\theta z} = 0, \qquad \sigma_{rz} = \mu\left(\frac{\partial u_r}{\partial z} + \frac{\partial u_z}{\partial r}\right),$$

and finally Eqs. (5) reduce to a PDE system of two equations (since the first Eq. of (5) vanishes) in the 2 unknowns u_r and u_z:

$$\frac{\partial \sigma_{rr}}{\partial r} + \frac{\sigma_{rr} - \sigma_{\theta\theta}}{r} + \frac{\partial \sigma_{rz}}{\partial z} = 0,$$
$$\frac{\partial \sigma_{zz}}{\partial z} + \frac{\partial \sigma_{rz}}{\partial r} + \frac{\sigma_{rz}}{r} = 0. \tag{8}$$

The 3D normal vector to an axis-symmetric surface $\Gamma_M = \{z = f_{\text{TOP}}(r)\}$ is $\boldsymbol{n} = (n_r, 0, n_z)$, leading to the following axis symmetric formulation of the stress-free boundary conditions $\boldsymbol{\sigma} \cdot \boldsymbol{n} = 0$:

$$\begin{pmatrix} \sigma_{rr} & 0 & \sigma_{rz} \\ 0 & \sigma_{\theta\theta} & 0 \\ \sigma_{rz} & 0 & \sigma_{zz} \end{pmatrix} \cdot \begin{pmatrix} n_r \\ 0 \\ n_z \end{pmatrix} = 0 \quad \Longrightarrow \quad \begin{cases} \sigma_{rr} n_r + \sigma_{rz} n_z = 0, \\ \sigma_{rz} n_r + \sigma_{zz} n_z = 0. \end{cases} \tag{9}$$

The 3D domain Ω_M and the surface Γ_M reduce to a 2D domain and a curve, respectively (that we continue to call Ω_M and Γ_M for simplicity), expressed as (see Figure 1):

$$\Omega_M = \big\{ (r,z) \in [0,+\infty[\times \mathbb{R} : z < f_{\text{TOP}}(r) \big\}, \tag{10}$$

$$\Gamma_M = \big\{ (r,z) \in [0,+\infty[\times \mathbb{R} : z = f_{\text{TOP}}(r) \big\}. \tag{11}$$

In summary, Eqs. (8) (with σ_{ij} expressed by Eqs. (7)) in the domain (10) with stress-free boundary conditions (9) on (11) and zero displacement at infinity constitute the 2D axis-symmetric thermo-poroelastic model.

By a similar argument, the axis-symmetric formulation of Eq. (2) becomes:

$$\frac{1}{r}\frac{\partial}{\partial r}\left(r \frac{\partial \phi_g}{\partial r} \right) + \frac{\partial^2 \phi_g}{\partial z^2} = -4\pi G \Delta\rho \quad \text{in } \mathbb{R}^2, \text{ with } \phi_g = 0 \text{ at infinity,}$$
$$\Delta g = -\frac{\partial \phi_g}{\partial z}. \tag{12}$$

2.3 Numerical method

Pressure, temperature and density changes induced by fluid circulation are computed using the TOUGH2 numerical code [23]. Starting from these quantities, ground deformation and gravity changes are solved through Equations (8) and (12) using a finite-difference ghost-point method developed in the context of elliptic problems [21] and recently extended to solve elastostatic equations in 2D plane strain configuration for unbounded domains [22]. Here, we extend the methods developed in [21, 22] to solve the axis symmetric formulations of Section 2.2.

The method consists of three stages: firstly, the unbounded domain problem is transformed in a bounded one by the coordinate transformation method. Secondly, the new set of equations and boundary conditions in the bounded domain is discretized by a finite-difference ghost-point approach. Finally, the discrete equations are solved by a proper geometric multigrid technique.
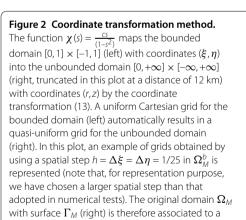
2.3.1 Coordinate transformation method

By the coordinate transformation method, the unbounded problem with variables (r, z) is mapped into a bounded one with new variables (ξ, η) as follows:
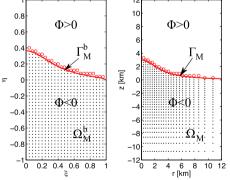
$$\begin{cases} r = \chi(\xi) \in [0, +\infty], \\ z = \chi(\eta) \in [-\infty, +\infty], \end{cases} \iff \begin{cases} \xi = \chi^{-1}(r) \in [0, 1], \\ \eta = \chi^{-1}(z) \in [-1, 1], \end{cases} \tag{13}$$

where $\chi : [-1, 1] \to [-\infty, +\infty]$ is a differentiable strictly increasing function in $]-1, 1[$ such that $\chi(0) = 0$ and $\lim_{s \to \pm 1} \chi(s) = \pm\infty$. Equations (8) and (12) (as well as the associated boundary conditions) are transformed according to (13), namely following the transformation of differential operators:

$$\frac{\partial}{\partial r} = \frac{1}{\chi'(\xi)} \frac{\partial}{\partial \xi} =: D_\xi, \qquad \frac{\partial}{\partial z} = \frac{1}{\chi'(\eta)} \frac{\partial}{\partial \eta} =: D_\eta. \tag{14}$$

The computational domain $\mathcal{C} = [0, 1] \times [-1, 1]$ is therefore discretized by a uniform Cartesian grid, which automatically results in a quasi-uniform grid for $[0, +\infty] \times [-\infty, +\infty]$ (see, for example, Figure 2). Imposing vanishing solution at infinity is equivalent to require zero Dirichlet boundary condition on $\partial \mathcal{C}$ for the transformed problem. The choice of the mapping function χ is crucial to define the mesh distribution in such a way a loss of accuracy of the numerical method is avoided. This is accomplished by two requirements: (i) the finest region of the quasi-uniform grid must cover the areas where the sources are concentrated, and (ii) the asymptotic behavior of the solution must be correctly captured. To satisfy the requirement (i), we observe that in the case of Eqs. (8) and (12) sources are concentrated where ΔP, ΔT and $\Delta \rho$ are different from zero. Since these quantities are evaluated by the hydrothermal model (detailed in Section 2.4), this area is certainly contained in Ω_H. Therefore, an acceptable mesh distribution should guarantee to cover a large

Figure 2 Coordinate transformation method. The function $\chi(s) = \frac{cs}{(1-s^2)}$ maps the bounded domain $[0, 1] \times [-1, 1]$ (left) with coordinates (ξ, η) into the unbounded domain $[0, +\infty] \times [-\infty, +\infty]$ (right, truncated in this plot at a distance of 12 km) with coordinates (r, z) by the coordinate transformation (13). A uniform Cartesian grid for the bounded domain (left) automatically results in a quasi-uniform grid for the unbounded domain (right). In this plot, an example of grids obtained by using a spatial step $h = \Delta\xi = \Delta\eta = 1/25$ in Ω_M^b is represented (note that, for representation purpose, we have chosen a larger spatial step than that adopted in numerical tests). The original domain Ω_M with surface Γ_M (right) is therefore associated to a domain Ω_M^b with surface Γ_M^b in the bounded domain (left). Equations (8) in Ω_M (as well as the stress-free boundary condition (9) on Γ_M) are transformed according to (14) into a new set of equations in Ω_M^b (with stress-free boundary conditions on Γ_M^b), solved by the finite-difference method described in Section 2.3.2. A level-set function ϕ is used to discriminate between internal points ($\phi < 0$, represented by black dots) and external points (see (15)). Among the latter, grid points close to the surface (ghost points, represented by red circles) are included to the discretized problem and a suitable value is assigned to them by enforcing boundary conditions (by the ghost-point method described in Section 2.3.2). The coordinate transformation method is used also to solve Eq. (12) in the domain $\mathbb{R}^2$ (then without a ghost-point level-set method).

region containing Ω_H by a fine grid. The resolution of the grid then decays going to infinity at the same order as the solution, to satisfy (ii). In practice, knowing the *a priori* asymptotic decay of solutions of Eqs. (8) and (12), it is possible to calibrate the mapping function in order to satisfy (ii) (namely, the gradient of the solution of the bounded problems does not have to develop singularities at the boundary of $[0, 1] \times [-1, 1]$). A good choice of mapping function is $\chi(s) = \frac{cs}{(1-s^2)}$. We refer the reader to [22] for an accurate discussion on the choice of a proper function of elasto-static problems. The parameter c regulates the length scale of the computational grid (and then the maximum resolution). In practice, to ensure a fine resolution in Ω_H, we impose that the spatial resolution at the boundary of Ω_H is half the resolution at the origin (where there is the minimum grid spacing). We choose c so that this condition is satisfied. In detail, we impose $\chi'(\chi^{-1}(\alpha)) = 2 \cdot \chi'(0)$, where α is the radius of the hydrothermal system (in our case $\alpha = 10$ km). If $m = 1$, after some algebra we obtain the condition:

$$c = \alpha \frac{\sqrt{2}}{2}.$$

By requirements (i) and (ii) the numerical method will achieve second order accuracy in a natural way, unlike the case when artificial truncation of the domain is used to assign zero displacement and zero potential boundary conditions.

2.3.2 Finite-difference ghost-point method

The discretization technique is applied to solve the transformed set of PDE's in the bounded domain (Ω_M^b for Eq. (8) and $[0, 1] \times [-1, 1]$ for Eq. (12)) discretized by a uniform Cartesian grid. A straightforward finite-difference scheme solves the transformed problem of (12), since it consists of a boundary value problem in a square domain discretized by a uniform Cartesian grid. This is not the case of the transformed problem of (8), where stress-free boundary conditions must be prescribed on an arbitrary topography, which is a part of the boundary of Ω_M^b. The domain Ω_M^b and surface Γ_M^b are implicitly described by a level-set function $\phi(\xi, \eta)$:

$$\Omega_M^b = \left\{ (\xi, \eta) \in \mathcal{C} : \phi(\xi, \eta) < 0 \right\}, \qquad \Gamma_M^b = \left\{ (\xi, \eta) \in \mathcal{C} : \phi(\xi, \eta) = 0 \right\}. \tag{15}$$

Observe that, if the topography function f_{TOP} is known, a level-set function can defined by $\phi = z - f_{\text{TOP}}(r)$. In the applications, the topography is often defined by a set of grid points (ξ_k, η_k) with $k = 1, \ldots, N_T$. A reasonably accurate level-set function can be obtained by $\phi(P) = \pm d(P, t)$, namely the signed distance between the point P and the line t passing through the two topography points (ξ_k, η_k) closest to P. The sign is determined by the mutual position between P and the two closest boundary points in such a way $\phi(P) < 0$ if and only if $P \in \Omega_M^b$.

Level-set methods are a powerful tool to implicitly describe moving geometries as well as complex topological changes [28]. Although in this paper we do not face moving geometries, the level-set function comes useful for two main reasons: (i) it provides accurate information, such as normal direction and curvature,

$$\boldsymbol{n} = \frac{\nabla \phi}{|\nabla \phi|}, \qquad \kappa = \nabla \cdot \boldsymbol{n}, \tag{16}$$

that can be adopted in the discretization technique to improve the accuracy of the method, and (ii) it allows us to provide a general numerical method that can be embedded in a more generic framework of time-dependent problems with (complex) moving geometries. Reason (i) is strictly related to the discretization technique adopted, which is described below.

The level-set function is able to discriminate between *internal* ($\phi < 0$) and *external* ($\phi \geq 0$) grid points. For each internal grid point Eqs. (8) are discretized using the standard central finite-difference discretization. In details, observe that the differential terms of Eqs. (8) (with σ components given by (7)) are a linear combination of:

$$\frac{\partial}{\partial \xi}\left(\gamma \frac{\partial w}{\partial \xi}\right), \qquad \frac{\partial}{\partial \xi}\left(\gamma \frac{\partial w}{\partial \eta}\right), \qquad \frac{\partial}{\partial \eta}\left(\gamma \frac{\partial w}{\partial \eta}\right), \qquad \frac{\partial}{\partial \eta}\left(\gamma \frac{\partial w}{\partial \xi}\right),$$
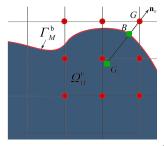
where γ is a smooth coefficient and $w = u_r$ or u_z. The finite-difference discretization of the previous terms is:

$$\frac{\partial}{\partial \eta}\left(\gamma \frac{\partial w}{\partial \eta}\right) \approx \frac{\gamma_{i+1/2,j}(w_{i+1,j} - W_{i,j}) - \gamma_{i-1/2,j}(w_{i,j} - w_{i-1,j})}{h^2},$$

$$\frac{\partial}{\partial \eta}\left(\gamma \frac{\partial w}{\partial \xi}\right) = \frac{\partial \gamma}{\partial \eta}\frac{\partial w}{\partial \xi} + \gamma \frac{\partial^2 w}{\partial \eta \partial \xi}$$

$$\approx \frac{(\gamma_{i+1,j} - \gamma_{i-1,j})(w_{i,j+1} - w_{i,j-1})}{4h^2} + \gamma_{i,j}\frac{w_{i+1,j+1} + w_{i-1,j-1} - w_{i+1,j-1} - w_{i-1,j+1}}{4h^2},$$

$$\frac{\partial}{\partial \xi}\left(\gamma \frac{\partial w}{\partial \eta}\right) = \frac{\partial \gamma}{\partial \xi}\frac{\partial w}{\partial \eta} + \gamma \frac{\partial^2 w}{\partial \eta \partial \xi}$$

$$\approx \frac{(\gamma_{i,j+1} - \gamma_{i,j-1})(w_{i+1,j} - w_{i-1,j})}{4h^2} + \gamma_{i,j}\frac{w_{i+1,j+1} + w_{i-1,j-1} - w_{i+1,j-1} - w_{i-1,j+1}}{4h^2},$$

$$\frac{\partial}{\partial \eta}\left(\gamma \frac{\partial w}{\partial \eta}\right) \approx \frac{\gamma_{i,j+1/2}(w_{i,j+1} - w_{i,j}) - \gamma_{i,j-1/2}(w_{i,j} - w_{i,j-1})}{h^2},$$

where $h = \Delta\xi = \Delta\eta$ is the (uniform) spatial step and $\gamma_{i+1/2,j} = (\gamma_{i,j} + \gamma_{i+1,j})/2$. Finite-difference discretization for an internal grid point involves then the surrounding grid nodes. Some of these surrounding points may lie outside of Ω_M^b, defining the so-called set of *ghost points*. Therefore the list of unknowns of the discrete linear system consists of the discrete values $\{u_r^P, u_z^P\}$, where the subscript P varies within the set of internal and ghost nodes. To close the linear system (*i.e.* to have a number of equations as much as the number of unknowns) two discrete equations must be generated for each ghost point G (to equate the two unknowns u_r^G and u_z^G). This discrete equations are recovered by prescribing the stress-free boundary condition on Γ_M^b with second order accuracy using the level-set function. In practice, referring to Figure 3, the discretization technique associated to a ghost point G consists of the following three stages.

- First we compute the projection B of G to the boundary by the level-set function. In details, we compute the outward unit normal vector $\boldsymbol{n}_G$ by discretizing Eq. (16) on G using a standard finite-difference scheme; then we apply the bisection method to solve the 1D nonlinear equation $\phi(B) = 0$ on the segment between points G and $G_1 = G - \sqrt{2}\,h\,\boldsymbol{n}_G$, with h being the spatial step.
- Then, we identify a nine-point stencil made by internal and ghost points, containing G and whose convex hull (the smallest convex set containing the stencil) contains B.

Figure 3 Stencil configuration. Nine-point stencil (red circles) associated with the ghost point G and used to compute the biquadratic interpolations of the terms composing the boundary conditions (9). Boundary conditions are then enforced on the boundary point B, computed by solving (via a bisection method) the 1D nonlinear equation $\phi(B) = 0$ on the segment between points G and $G_1 = G - \sqrt{2}\,h\,\boldsymbol{n}_G$, with h being the spatial step.

In Figure 3 the nine-point stencil is represented by red circles. Although there are different stencils satisfying these conditions, an appropriate choice will often avoid numerical instabilities in the solution (see [22] for more details and examples).

- Stress-free boundary conditions (9) are then imposed on B, providing then the following two equations of the linear system for u_r^G and u_z^G:

$$
\begin{cases}
(\tilde{\sigma}_{rr} \frac{\partial \tilde{\phi}}{\partial r} + \tilde{\sigma}_{rz} \frac{\partial \tilde{\phi}}{\partial z})|_B = 0, \\
(\tilde{\sigma}_{rz} \frac{\partial \tilde{\phi}}{\partial r} + \tilde{\sigma}_{zz} \frac{\partial \tilde{\phi}}{\partial z})|_B = 0,
\end{cases}
\tag{17}
$$

where $\tilde{\sigma}_{rr}$, $\tilde{\sigma}_{rz}$, $\tilde{\sigma}_{zz}$ and $\tilde{\phi}$ are the biquadratic interpolant on the nine-point stencil of σ_{rr}, σ_{rz}, σ_{zz} and ϕ, respectively.

2.3.3 Multigrid solver
The discrete linear systems involving the unknowns $\{u_r^P, u_z^P\}$, with P varying within the sets of internal and ghost points, is solved by an efficient geometric multigrid solver, which is an extension of the multigrid approach proposed in [22] (to which the reader is referred for more details).

2.4 Hydrothermal model
The circulation of hot fluids in the hydrothermal system is modelled by TOUGH2 [23], a well-known software to simulate multiphase multicomponent fluid flow and heat transfer in porous media. For a generic multiphase fluid with k components a set of $k+1$ equations (k mass equations and one energy equation) is solved. The $k + 1$ equations can be resumed as follows [23]:

$$
\frac{\partial Q_\alpha}{\partial t} + \nabla \cdot F_\alpha - q_\alpha = 0, \quad \alpha = M_1, \ldots, M_k, E, \text{ in } \Omega_H,
\tag{18}
$$

where $Q_\alpha = Q_\alpha(\vec{x}, t)$ is the accumulation term, $F_\alpha = F_\alpha(\vec{x}, t)$ the flux and $q_\alpha = q_\alpha(\vec{x}, t)$ the source (or sink) term. Subscript $\alpha = M_i$ or E refers to the mass balance equation of the i-th component or to the energy balance equation, respectively. Accumulation terms and fluxes for the mass balance equations $\alpha = M_i$ and energy equation $\alpha = E$ are

$$
Q_{M_i} = \phi \sum_\beta \rho_\beta S_\beta \chi_\beta^i, \qquad F_{M_i} = \sum_\beta \chi_\beta^i F_\beta,
\tag{19}
$$

$$
Q_E = \phi \sum_\beta (\rho_\beta e_\beta S_\beta) + (1 - \phi)\rho_r C_r T, \qquad F_E = -\lambda \nabla T + \sum_\beta h_\beta F_\beta,
\tag{20}
$$

Table 1 Description of the quantities appearing in Eqs. (19)-(20)

Notation	Description	Status
$\phi(\vec{x})$	Porosity	Assigned
$\rho_r(\vec{x})$	Density of the rock	Assigned
$C_r(\vec{x})$	Specific heat of the rock	Assigned
$\lambda(\vec{x})$	Thermal conductivity of the rock	Assigned
$K(\vec{x})$	Permeability of the rock	Assigned
$\hat{g}$	Gravity acceleration	Assigned
$\rho_\beta(\vec{x}, t)$	Density of the phase β	Unknown
$S_\beta(\vec{x}, t)$	Saturation of the phase β	Unknown
$\chi_\beta^i(\vec{x}, t)$	Mass fraction of the i-th component in the phase β	Unknown
$e_\beta(\vec{x}, t)$	Internal energy of the phase β	Unknown
$h_\beta(\vec{x}, t)$	Enthalpy of the phase β	Unknown
$k_\beta(\vec{x}, t)$	Relative permeability of the phase β	Unknown
$\eta_\beta(\vec{x}, t)$	Viscosity of the phase β	Unknown
$P_\beta(\vec{x}, t)$	Pressure of the phase β	Unknown
$T(\vec{x}, t)$	Temperature	Unknown

Dependence on $\vec{x}$ and/or t is also highlighted in the first column. All quantities that do not depend on time are *a priori* assigned. The subscript β refers to the liquid ($\beta = l$) or gas ($\beta = g$) phase.

where the subscript $\beta = l$ or g refers to the liquid or gas phase, respectively, and $F_\beta = \frac{K k_\beta \rho_\beta}{\mu_\beta}(\nabla P_\beta - \rho_\beta \hat{g})$ is the fluid flux of the phase β, based on the Darcy law. Refer to Table 1 for the description of the quantities introduced in Eqs. (19)-(20). Quantities depending on time constitute the unknown variables of the model. A suitable set of $k + 1$ primary variables is chosen among the unknowns, and, to close the system (18), the remaining variables (secondary variables) are expressed in terms of the primary variables. Each combination of values of primary variables then identifies uniquely the state of the fluid. The functional dependences of the secondary variables with respect to the primary variables are based on the Equations Of State (EOS), which depend on the number and nature of components. In the simulations considered in this paper, we use $k = 1$ or $k = 2$ to simulate pure water (EOS1 module of TOUGH2) or water and carbon dioxide (EOS2 module of TOUGH2) injection, respectively.

We call $\Omega_H \subset \mathbb{R}^3$ the spatial domain in which we solve Eq. (18) (the domain of the hydrothermal model). Due to the axis-symmetric configuration of the problem, the domain can be expressed in terms of the radial distance $r = \sqrt{x^2 + y^2}$ and the vertical variable z, as $\Omega_H = \{0 \le r \le R, z_{\min} \le z < f_{\text{TOP}}(r)\}$, where $f_{\text{TOP}}(r)$ represents the topography function (see Figure 1). Since TOUGH2 does not account for infinite domains, Ω_H differs from Ω_M and is truncated at a radial distance of $r = R$ and a depth of $z = z_{\min}$. On the portion of the ground surface within a radial distance $r \le R$, Γ_H, atmospheric (Dirichlet) boundary conditions for pressure and temperature are prescribed.

In multi-phase system, each phase may be at a different pressure P_β due to interfacial curvature and capillary forces. The difference between the gas and liquid pressures is referred as capillary pressure P_c. Capillary pressure and relative permeabilities k_β, $\beta = l, g$, are usually posed as a function of the liquid saturation S_l. In this paper we use the capillary pressure and relative permeabilities set according to the following Brooks-Corey functions [29]:

$$P_c = P_0 S_e^2,$$

$$k_l = S_e^4, \tag{21}$$

$$k_g = \left(1 - S_e^2\right)(1 - S_e)^2,$$

$$S_e = \frac{S_l - S_{lr}}{1 - S_{lr} - S_{gr}},$$

where S_e is the effective saturation, $S_{lr} = 0.33$ the residual liquid saturation and $S_{gr} = 0.05$ the residual gas saturation.

3 Simulation of unrest at Campi Flegrei

The method is applied at the Campi Flegrei area to simulate an unrest caused by a deep injection of hot fluid in the caldera [12–14]. The ground surface is represented by a profile of the real topography of the Campi Flegrei area computed from the Digital Elevation Model of the Shuttle Radar Topography Mission (Figure 4). The computational domain Ω_H for the TOUGH2 simulations extends up to a radial distance of $R = 10$ km and a depth of $z_{\min} = 1.5$ km computed from the intersection between the ground surface and the axis of symmetry. The domain Ω_H was discretized in the radial direction by a set of logarithmically spaced nodes with a horizontal resolution starting from 61.33 m along the axis of symmetry and decreasing to 470 m at the external boundary. Vertically, the domain was divided into 33 equally spaced layers, which corresponds to a resolution of 45 m/layer. This discretization leads to 2,400 cells.

In the thermo-poroelastic and gravity models the domain extends toward infinity (Figure 1), warranting zero displacement and potential. The computational grid is vertex-centered and has a maximum resolution of $\Delta r = \Delta z = 38.76$ m at $r = z = 0$.

Firstly, TOUGH2 is run to evaluate temperature, pressure and density variations with respect to their initial distributions, which, then, are fed into the thermo-poroelastic solver to compute the deformation and gravity changes. Due to the different grids adopted, these quantities are interpolated from the TOUGH2 grid to the thermo-poroelastic solver nodes.

In all the TOUGH2 simulations, atmospheric boundary conditions $P = 0.1$ MPa and $T = 20°C$ are prescribed on the surface $\Gamma_H = \{z = f_{\mathrm{TOP}}(r)\}$, while adiabatic and impervious
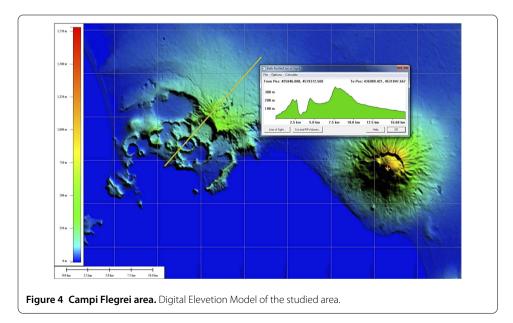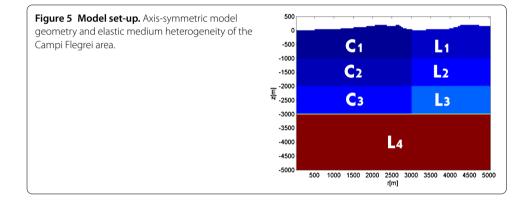

Figure 4 Campi Flegrei area. Digital Elevation Model of the studied area.

Table 2 Rock properties used in calculations of the hydrothermal model

Density	2000 kg/m^3
Permeability	10^{-14} m^2
Conductivity	2.8 W m^{-1} K^{-1}
Porosity	0.2
Specific heat	1000 J kg^{-1} K^{-1}

Table 3 Elastic properties of the medium

Region	Rigidity [GPa]	Poisson ratio
L1	4	0.25
C1	2.3	0.33
L2	5	0.25
C2	3.6	0.33
L3	6.5	0.25
C3	5	0.33
L4	20	0.25

Figure 5 Model set-up. Axis-symmetric model geometry and elastic medium heterogeneity of the Campi Flegrei area.

conditions are set on the remaining boundaries $\{r = R\}$ and $\{z = z_{\min}\}$, except at the inlet near the symmetry axis, where inflow boundary conditions are prescribed.

Values of the hydrological and thermal properties of rocks are defined on the basis of literature data [12, 14] (Table 2). The elastic medium properties are defined on the basis of tomographic studies [30], which depict the heterogeneity of the shallow structure of Campi Flegrei (Table 3). Following [31], the shallow area of the medium is divided into three horizontal layers having a thickness of 1 km. The inner caldera is modelled as a 3 km wide cylinder, coaxial with the axis of symmetry, with an internal variation of the elastic parameters. A further layer extends from 3 km depth to the bottom of the (infinite) computational domain (Figure 5). The thermal expansion coefficient α is $10^{-5} K^{-1}$ and the Biot-Willis coefficient α_{BW} is $(1 - K/K_s)$, where K is the isothermal drained bulk modulus (5 GPa) and K_s is the bulk modulus of the solid constituent (30 GPa) [12].

Although hydrothermal fluids are not pure substances, but generally mixtures of several mass components or chemical species, the dominant fluid component is usually water, and it is often reasonable to ignore other components. However, in volcanic regions the aqueous phase generally contains also dissolved incondensable gases, such as CO_2. To investigate the effect of a CO_2 component in water, two different scenarios are investigated, simulating: (1) a pure water injection using the TOUGH2/EOS1 module, which models a water system in its liquid, vapor, and two-phase states; (2) a mixture of water

and carbon dioxide injection using the TOUGH2/EOS2 module, which accounts for the non-ideal behavior of gaseous CO_2 and dissolution of CO_2 in the aqueous phase.

We observe that the depth of Ω_H is chosen in such a way the focus of the simulations is on the shallower hydrothermal activity, in order to maintain temperature and pore pressure within the range considered by TOUGH2, which does not take into account super-critical fluids. Therefore, in all the simulations of this paper we investigate only sub-critical fluids.

Observe that we do not aim to simulate the subsidence period following the main unrest phase, and therefore the simulation is confined to the first years of unrest.

3.1 Injection rates

In the following sections two scenarios will be studies: pure water injection and water and carbon dioxide injection. The injection rates adopted in the scenario of water and carbon dioxide injection are obtained from previous works according to geochemical data collected at the CFc and providing a good matching to observed data [12, 18, 19]. The injection rates adopted for the scenario of pure water injection are chosen in such a way the total mass of fluid injected is the same for both scenarios.
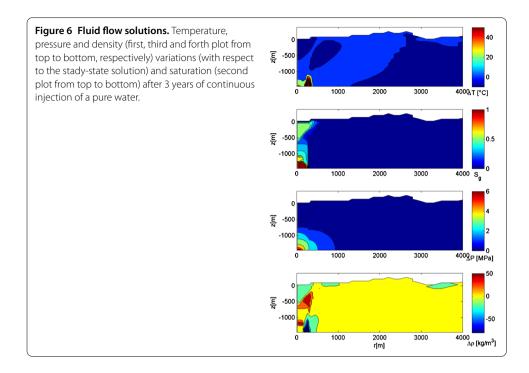
3.2 Pure water injection

In this first scenario the fluid is composed of pure water, whose properties and phase transitions are calculated based on the thermodynamic conditions, according to the steam table equation [32]. Initial conditions are obtained reaching a steady-state solution by simulating a 5 thousand year long phase with a deep injection of hot water with a constant flux rate of 39.4 kg/s at temperature of 350°C. The fluid is injected in a 150 m wide inlet located at the bottom of the domain around the symmetry axis. This extent has been estimated from the area affected by fumaroles activity [18].
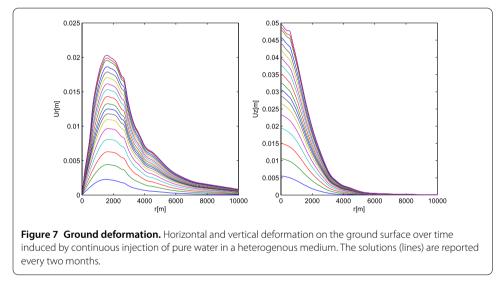
The unrest is simulated increasing the flux rate to 140.05 kg/s for 3 years. The distributions of saturation and pressure, temperature and density changes at the end of the unrest with respect to the steady-state initial conditions are displayed in Figure 6. Temperature changes are restricted near the inlet, whereas pressure changes of a few MPa are distributed in a larger area. The saturation shows that the fluid is gas-saturated at the base and a two-phase fluid reaches the ground surface. The saturation distribution controls the fluid density, which shows negative variations at the edge of the inlet and positive variations at a mid-depth of the domain. Using these solutions the evolution of ground deformation and gravity changes are then evaluated.

The deformation field (Figure 7) computed solving Eq. (1) resembles the patterns obtained in [12–14], although there are some discrepancies in the amplitudes, likely arising from the medium heterogeneity rock properties and the single component injection. It is similar to deformation field arising from spherical point pressure sources. During the unrest the deformation monotonously increases reaching an amplitude of 2.1 cm and 5.0 cm in the horizontal and vertical component, respectively.

A comparison with a homogeneous model, in which the rigidity is 2 GPa and the Poisson's ratio is 0.3 is performed. An enhancement in the deformation field is observed since the rigidity is lower with respect to the heterogeneous model (Figure 8).

The deformations are accompanied by significant gravity changes induced by the fluid density variations. The gravity changes computed at the axis of symmetry on the ground surface (Figure 6) increase almost linearly through time and reach about 135 μGal after
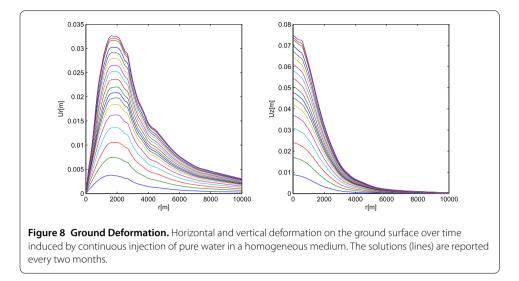
Figure 6 Fluid flow solutions. Temperature, pressure and density (first, third and forth plot from top to bottom, respectively) variations (with respect to the stady-state solution) and saturation (second plot from top to bottom) after 3 years of continuous injection of a pure water.

Figure 7 Ground deformation. Horizontal and vertical deformation on the ground surface over time induced by continuous injection of pure water in a heterogenous medium. The solutions (lines) are reported every two months.

3 years of constant injection. The ratio $\Delta g/\Delta h$ increases monotonously reaching a value of about 27 μGal/cm. These results are in fully agreement with those obtained by Coco *et al.* [33] using the HYDROTHERM flow code [23].

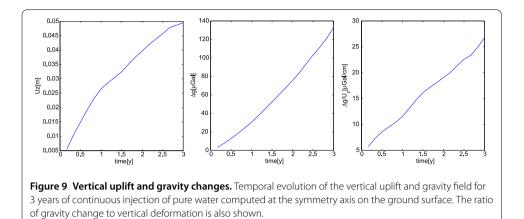### 3.3 Water and carbone dioxide injection

In this second scenario the fluid is a mixture of water and carbon dioxide. The initial conditions are achived by injecting for 5 thousand years a fluid at temperature of 350°C composed of a water component with a flux rate of 27.8 kg/s and a CO_2 component with a flux rate of 11.6 kg/s. Then, the unrest is simulated increasing the flux rates to 70.6 kg/s for the water and to 69.4 kg/s for the CO_2. The distributions of saturation and pressure, temperature, and density variations after 3 years from the unrest are displayed in Figure 10.

Figure 8 Ground Deformation. Horizontal and vertical deformation on the ground surface over time induced by continuous injection of pure water in a homogeneous medium. The solutions (lines) are reported every two months.
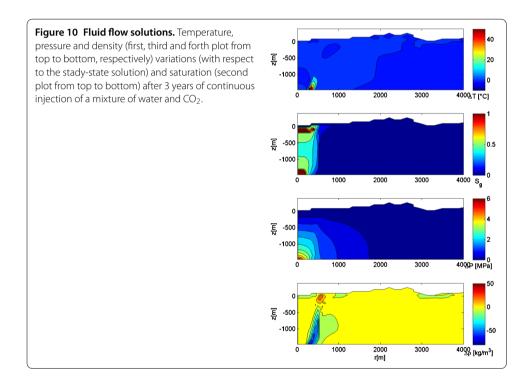
The distributions are quite different with respect to the first scenario, when only water is injected (Figure 6). The pressure changes affect a wider area, whereas the temperature changes are almost similar to the previous scenario. The saturation shows two areas of gas-saturated zones, one at the inlet and the other one below the ground surface. The fluid density variations are almost negative at the edge of the rising plume, where liquid phase is substituted by gas phase. The pressure and temperature changes greatly affect the ground deformation as shown in Figure 11. These behaviors are in agreement with the results obtained in [12].

Under a constant injection rate, the temporal pattern of ground deformation shows an exponential increase (Figure 12). After 3 years of continuous fluid injection the horizontal deformation reaches a maximum value of about 3 cm at 1500 m from the symmetry axis and the vertical uplift attains about 8.5 cm at the simmetry axis. It is worth of noting that the amplitude of the displacement is enhanced with respect to the first scenario when only pure water is injected. Contrarily, Troiano *et al.* found in [14] that similar deformations are obtained injecting either water or a mixuture of water and CO_2. This discrepancy among the results could be ascribed to the different ratio between water and carbone dioxide components. Indeed, Troiano *et al.* used in [14] a flux rate of 92.6 kg/s for water and of 9.26 kg/s for CO_2, leading to a molar ratio of 0.04, which is one tenth of the value used in our simulations. The effect of the CO_2 component is much more evident by comparing the results on gravity changes (Figures 9, 12).

In presence of CO_2 the temporal variations of the gravity field caused by changes in the average fluid density (Figure 10) show a peculiar pattern. A positive increase, which reaches a maximum value of about 20 μGal, is observed until 1.2 years after the onset of the unrest. Then, a decreasing trend marks the evolution of the gravity changes. This behaviour could be attributed to the negative density variations generated by the ascent of the gas-rich fluids (Figure 10). Most intriguing is the controversial trend between the gravity changes and the vertical deformation. Their ratio ranges between -4.5 and 4.5 μGal/cm. However, these results are in agreement with previous works, such as [34].

Figure 9 Vertical uplift and gravity changes. Temporal evolution of the vertical uplift and gravity field for 3 years of continuous injection of pure water computed at the symmetry axis on the ground surface. The ratio of gravity change to vertical deformation is also shown.

Figure 10 Fluid flow solutions. Temperature, pressure and density (first, third and forth plot from top to bottom, respectively) variations (with respect to the stady-state solution) and saturation (second plot from top to bottom) after 3 years of continuous injection of a mixture of water and CO_2.

4 Conclusion

A finite-difference ghost-point method for solving the elasto-static and Poisson equations on an arbitrary unbounded domain has been presented. The proposed strategy, which adopts the coordinate transformation method, has been applied to thermo-poroelastic models to evaluate deformation and gravity changes in volcanic areas. The method has been coupled with the TOUGH2 code to investigate the role of pressure, temperature and density changes on the geophysical observables. The results from two scenarios have been compared in order to explore the effect of the presence of carbon dioxide in the fluid mixture. Although the total flux rate is similar in both scenarios, the presence of CO_2 strongly alter the solutions. Particularly, the injection of the CO_2 engenders an enhancement in the deformation field and perturbs the temporal evolution of the gravity changes. This last feature could be a useful signature to constrain the relative ratio between water and carbon dioxide content. It turns out that the ratio between gravity and vertical deformation de-
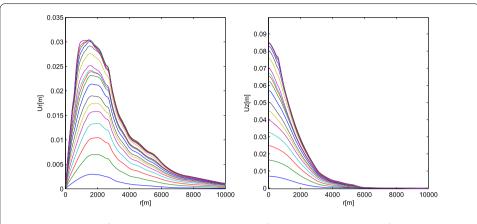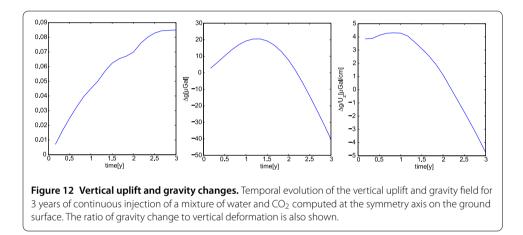
Figure 11 Ground Deformation. Horizontal and vertical deformation on the ground surface over time induced by continuous injection of a mixture of water and CO_2 in a heterogenous medium. The lines refer to solutions computed every two months.

Figure 12 Vertical uplift and gravity changes. Temporal evolution of the vertical uplift and gravity field for 3 years of continuous injection of a mixture of water and CO_2 computed at the symmetry axis on the ground surface. The ratio of gravity change to vertical deformation is also shown.

creases for higher ratios of CO_2/H_2O. The comparisons between gravity and deformation may help to discriminate between injection with or without carbon dioxide content and to provide inferences on the nature of the source. Since unrest periods are accompanied by increases of the CO_2/H_2O ratio, a decrease in the ratio between gravity and vertical deformation could help in detecting the onset of unrest phases. Moreover, our findings seem able to justify what observed in some volcanic regions, where major gravity changes appear without any significant deformation. In many volcanoes worldwide, there are evidences that the ratio between gravity and height changes is far beyond what could be predicted by simple models, in which volume and pressure changes in a magma chamber are considered. When significant gravity changes occur without any significant deformation, or vice versa, it is often difficult, if not impossible, to jointly explain the observations using the popular Mogi model. Our results may provide an alternative explanation to the observations and help in resolving the controversy between geodetic and gravity observations as a volcano moves from rest to unrest state.

However, there are some limitations of the model presented in this paper that must be considered. The shallow hydrothermal system is only 1.5 km deep, while a deeper model is more realistic to represent volcanic areas [7, 17]. The shallow injection depth considered in this paper is constrained by the range of applicability of TOUGH2, which does not account

for supercritical fluids. Some recent models investigated the influence of super-critical fluids to the results, allowing to consider deeper domains [35]. The 2D axi-symmetric representation may not be able to describe the complex 3D network that characterises caldera systems. However, to a first approximation calderas present a radial structure and then can be approximated by the axis symmetric assumption. The one-way coupling between the hydrothermal model and the thermo-poroelastic model represents a reasonable simplification when a short period of unrest is simulated, but it is not adequate for simulations of longer processes, where stress and strain alterations may induce a significant variation in the relevant hydrological parameters (permeability, porosity), modifying the long term processes of fluid flows in the porous medium and then the associated geophysical signals [36, 37].

The effects of these limitations may be reduced by considering a more realistic fully coupled 3D model that accounts for super-critical fluids. The implementation of a more effective simulator is part of our future investigations, with the aim to extend the simulation to more realistic cases of multi-component fluids.

Competing interests

The authors declare that they have no competing interests.

Authors' contributions

All the authors coordinated the writing of the paper and the research it is based on; numerical simulations were undertaken by GC and AC; AC developed the numerical code under the supervision of GR. All authors read and approved the final manuscript.

Author details

^{1}Department of Mechanical Engineering and Mathematical Sciences, Oxford Brookes University, Wheatley campus, Oxford, OX331HX, United Kingdom. ^{2}Department of Earth Sciences, University of Bristol, Wills Memorial Building, Queen's Road, Clifton, Bristol, BS81RJ, United Kingdom. ^{3}Istituto Nazionale di Geofisica e Vulcanologia, Piazza Roma, Catania, 95125, Italy. ^{4}Università di Catania, Viale A. Doria, Catania, 95125, Italy.

References

1. Del Negro C, Currenti G, Solaro G, Greco F, Pepe A, Napoli R, Pepe S, Casu F, Sansosti E. Capturing the fingerprint of Etna volcano activity in gravity and satellite radar data. Sci Rep. 2013;3:3089. doi:10.1038/srep03089.
2. Bonafede M, Dragoni M, Quareni F. Displacement and stress fields produced by a centre of dilatation and by a pressure source in a viscoelastic half-space: application to the study of ground deformation and seismic activity at Campi Flegrei, Italy. Geophys J R Astron Soc. 1986;87:455-85.
3. Bianchi R, Coradini A, Federico C, Giberti G, Lanciano P, Pozzi JP, Sartoris G, Scandone R. Modeling of surface deformation in volcanic areas: the 1970-1972 and 1982-1984 crises of Campi Flegrei, Italy. J Geophys Res. 1987;92(B13):14139-50.
4. De Natale G, Pingue F, Allard P, Zollo A. Geophysical and geochemical modelling of the 1982-1984 unrest phenomena at Campi Flegrei caldera (southern Italy). J Volcanol Geotherm Res. 1991;48:199-222.
5. Dzurisin D, Savage JC, Fournier RO. Recent crustal subsidence at Yellowstone caldera, Wyoming. Bull Volcanol. 1990;52(4):247-70.
6. Watson IM, Oppenheimer C, Voight B, Francis PW, Clarke A, Stix J, Miller A, Pyle DM, Burton MR, Young SR, et al.. The relationship between degassing and ground deformation at Soufriere Hills Volcano, Montserrat. J Volcanol Geotherm Res. 2000;98(1):117-26.
7. Gottsmann J, Camacho AG, Tiampo KF, Fernández J. Spatiotemporal variations in vertical gravity gradients at the Campi Flegrei caldera (Italy): a case for source multiplicity during unrest? Geophys J Int. 2006;167:1089-96.
8. Chiodini G, Vilardo G, Augusti V, Granieri D, Caliro S, Minopoli C, Terranova C. Thermal monitoring of hydrothermal activity by permanent infrared automatic stations: results obtained at Solfatara di Pozzuoli, Campi Flegrei (Italy). J Geophys Res. 2007;112:B12206. doi:10.1029/2007JB005140.
9. Gottsmann J, Camacho AG, Martí J, Wooller L, Fernández J, Garcia A, Rymer H. Shallow structure beneath the Central Volcanic Complex of Tenerife from new gravity data: implications for its evolution and recent reactivation. Phys Earth Planet Inter. 2008;168(3):212-30.
10. Hutnak M, Hurwitz S, Ingebritsen SE, Hsieh PA. Numerical models of caldera deformation: effects of multiphase and multicomponent hydrothermal fluid flow. J Geophys Res. 2009;114:B04411. doi:10.1029/2008JB006151.

11. Ingebritsen SE, Geiger S, Hurwitz S, Driesner T. Numerical simulation of magmatic hydrothermal systems. Rev Geophys. 2010;48:RG1002. doi:10.1029/2009RG000287.

12. Rinaldi A, Todesco M, Bonafede M. Hydrothermal instability and ground displacement at the Campi Flegrei caldera. Phys Earth Planet Inter. 2010;178:155-61.

13. Rinaldi A, Todesco M, Bonafede M, Vandemeulebrouck MJ, Revil A. Electrical conductivity, ground displacement, gravity changes, and gas flow at Solfatara crater (Campi Flegrei caldera, Italy): results from numerical modeling. J Volcanol Geotherm Res. 2011;207:93-105.

14. Troiano A, Di Giuseppe MG, Petrillo Z, Troise C, De Natale G. Ground deformation at calderas driven by fluid injection: modelling unrest episodes at Campi Flegrei (Italy). Geophys J Int. 2011;187:833-47.

15. Troise C, De Natale G, Pingue F, Tammaro U, De Martino P, Obrizzo F, Boschi E. A new uplift episode at Campi Flegrei caldera (southern Italy): implications for unrest interpretation and eruption hazard evaluation in Caldera Volcanism: analysis, modelling and response. Dev Volcanol. 2008;10:375-92.

16. De Martino P, Tammaro U, Obrizzo F. GPS time series at Campi Flegrei caldera (2000-2013). Ann Geophys. 2014;57(2):S0213. doi:10.4401/ag-6431.

17. Amoruso A, Crescentini L, Sabbetta I, De Martino P, Obrizzo F, Tammaro U. Clues to the cause of the 2011-2013 Campi Flegrei caldera unrest, Italy, from continuous GPS data. Geophys Res Lett. 2014;41:3081-8. doi:10.1002/2014GL059539.

18. Chiodini G, Todesco M, Caliro S, Gaudio CD, Macedonio G, Russo M. Magma degassing as a trigger of bradyseismic events: the case of Phlegrean fields (Italy). Geophys Res Lett. 2003;30:1434-7.

19. Todesco M, Rinaldi AP, Bonafede M. Modeling of unrest signals in heterogeneous hydrothermal systems. J Geophys Res. 2010;115:B09213. doi:10.1029/2010JB007474.

20. Rutqvist J. Status of the TOUGH-FLAC simulator and recent applications related to coupled fluid flow and crustal deformations. Comput Geosci. 2011;37:739-50. doi:10.1016/j.cageo.2010.08.006.

21. Coco A, Russo G. Finite-difference ghost-point multigrid methods on Cartesian grids for elliptic problems in arbitrary domains. J Comput Phys. 2013;241:464-501.

22. Coco A, Currenti G, Del Negro C, Russo G. A second order finite-difference ghost-point method for elasticity problems on unbounded domains with applications to volcanology. Commun Comput Phys. 2014;16:983-1009.

23. Pruess K, Oldenburg C, Moridis G. TOUGH2 User's Guide, Version 2.0. Paper LBNL-43134, Lawrence Berkeley National Laboratory, Berkeley, CA, USA. 1999.

24. Chiodini G, Frondini F, Cardellini C, Granieri D, Marini L, Ventura G. CO2 degassing and energy release at Solfatara volcano, Campi Flegrei, Italy. J Geophys Res. 2001;106:16213-21.

25. Jaeger JC, Cook NGW, Zimmerman RW. Fundamentals of rock mechanics. 4th ed. Oxford: Blackwell Publishing; 2007.

26. Fung YC. Foundations of solid mechanics. Englewood Cliffs: Prentice-Hall; 1965.

27. Currenti G. Numerical evidences enabling to reconcile gravity and height changes in volcanic areas. Geophys J Int. 2014; 197(1):164-73. doi:10.1093/gji/ggt507.

28. Osher S, Fedkiw R. Level set methods and dynamic implicit surfaces. New York: Springer; 2002.

29. Brooks A, Corey AT. Hydraulic properties of porous media. Colorado State 599 University Hydrology. Paper No. 3, Fort Collins, Colorado, USA. 1964.

30. Zollo A, Judenherc S, Auger E, D'Auria L, Virieux J, Capuano P, Chiarabba C, De Franco R, Makris J, Michelini A, Musacchio G. Evidence for the buried rim of Campi Flegrei caldera from 3-d active seismic imaging. Geophys Res Lett. 2003;30:2002. doi:10.1029/2003GL018173.

31. Trasatti E, Giunchi C, Bonafede M. Structural and rheological constraints on source depth and overpressure estimates at the Campi Flegrei caldera, Italy. J Volcanol Geotherm Res. 2005;144:105-18.

32. Committee IF. A formulation of the thermodynamic properties of ordinary water substance. ICF Secretariat. 1967.

33. Coco A, Currenti G, Gottsmann J, Del Negro C, Russo G. Geophysical changes in hydrothermal-volcanic areas: a finite-difference ghost-cell method to solve thermo-poroelastic equations. Progress in Industrial Mathematics at ECMI 2014. In print.

34. Todesco M, Berrino G. Modeling hydrothermal fluid circulation and gravity signals at the Phlegraean fields caldera. Earth Planet Sci Lett. 2005;240:328-38. doi:10.1016/j.epsl.2005.09.016.

35. Afanasyev A, Costa A, Chiodini G. Investigation of hydrothermal activity at Campi Flegrei caldera using 3D numerical simulations: extension to high temperature processes. J Volcanol Geotherm Res. 2015;299:68-77.

36. Neuzil CE. Hydromechanical coupling in geologic processes. Hydrogeol J. 2003;11(1):41-83.

37. Rutqvist J, Wu Y-S, Tsang C-F, Bodvarsson G. A modeling approach for analysis of coupled multiphase fluid flow, heat transfer, and deformation in fractured porous rock. Int J Rock Mech Min Sci Geomech Abstr. 2002;39:429-42.